Interseries dipole transitions from yellow to green excitons in cuprous oxide

Patric Rommel* and Jörg Main
Institut für Theoretische Physik 1, Universität Stuttgart, 70550 Stuttgart, Germany

Sjard Ole Krüger and Stefan Scheel
Institut für Physik, Universität Rostock, Albert-Einstein-Straße 23-24, 18059 Rostock, Germany

(Received 30 April 2021; revised 15 July 2021; accepted 10 August 2021; published 23 August 2021)

We study dipole interseries transitions between the yellow and green exciton series in cuprous oxide including the complex valence-band structure. To this end, we extend previous studies of the spectrum of complex green exciton resonances [P. Rommel, P. Zielinski, and J. Main, Phys. Rev. B **101**, 075208 (2020)] to optical transitions between different exciton states in addition to transitions from the crystal ground state. This allows us to augment the calculations on interseries transitions using a hydrogenlike model [S. O. Krüger and S. Scheel, Phys. Rev. B **100**, 085201 (2019)] by a more comprehensive treatment of the valence-band structure.

DOI: 10.1103/PhysRevB.104.085204

I. INTRODUCTION

Cuprous oxide has long been a very interesting system for the study of excitons. Indeed, it was in this material that excitons were first observed [1,2], and in which bound states with principal quantum numbers up to $n = 25$ have been detected [3]. This abundance of known resonances allows for very precise tests of theoretical models, and allows one to probe the influence of intricate details of the band structure on the formation of excitons.

Most of the work in the literature focuses on the yellow series, which is formed by electrons in the lowest Γ_6^+ conduction band and holes in the uppermost Γ_7^+ valence band [4–6]. The green excitons, on the other hand, are formed by holes in the Γ_8^+ valence band [7–9]. For principal quantum numbers $n \geqslant 2$, they are located at energies above the band gap of the yellow excitons, and couple to the yellow continuum states. Thus, even without taking phonon coupling into account, the green excitons above the yellow band gap are no longer bound states with infinite lifetimes, but quasibound resonances with finite lifetimes. Recently, the location of the green exciton resonances has been calculated [10] using the complex-scaling method [11,12].

Motivated by the aim to identify promising experimentally accessible dipole transitions for the coherent manipulation of Rydberg excitons [13,14] and the generation of giant optical nonlinearities [15], interseries transitions between the yellow and green, respectively, yellow and blue, exciton series have been investigated using a hydrogenlike model for the exciton interaction [16]. The interseries transitions, i.e., those between different exciton series, have the distinct advantage over intraseries transitions, i.e., transitions within a single exciton series, by providing a more accessible choice of interrogation wavelengths. To wit, transition wavelengths between adjacent Rydberg states within the same series scale as n^3 and quickly approach the millimeter range, whereas the wavelength limit for interseries transitions is set by the energy difference between bands, which are typically in the near to mid IR. In this paper, we investigate interseries dipole transitions between the yellow and green exciton series, while taking into account the complex structure of the valence band [5,17] as well as central-cell corrections [18–22]. As our focus is not on optical transitions where the exciton is created from the crystal ground state, but rather on transitions between different exciton states, this requires an extensive modification of the scheme for calculating the oscillator strengths.

The paper is organized as follows. First, we present the numerical calculation of the relevant exciton states using a unified Hamiltonian describing both the yellow and green series in Sec. II. Using the calculated eigenvalues and eigenvectors, we derive the dipole transition matrix elements in Sec. III. In Sec. IV, we present and discuss our results on interseries dipole transitions and absorption spectra. We finish the paper with some concluding remarks in Sec. V.

II. THE SPECTRUM OF YELLOW AND GREEN EXCITONS

In this section we briefly recapitulate and extend our technique for calculating the bound yellow exciton states and the unbound green exciton resonances by using a complete basis set and the complex-coordinate rotation method. For both the yellow and green series, we take the valence-band structure and central-cell corrections into account. The knowledge of the precise states is the prerequisite for the computation of interseries dipole transitions in Secs. III and IV.

A. Hamiltonian

The description of excitons follows the line of arguments laid out in Ref. [10]. For the investigation of interseries transitions between yellow and green exciton states, we use the

*patric.rommel@itp1.uni-stuttgart.de

unified description of the two series given by the Hamiltonian [5,10,17,18,23]

$$H = E_g + \frac{\gamma_1'}{2m_0}\boldsymbol{p}^2 + H_b(\boldsymbol{p}) - \frac{e^2}{4\pi\varepsilon_0\varepsilon|\boldsymbol{r}|} + H_{CCC}, \quad (1)$$

with the valence-band corrections to the kinetic energy

$$\begin{aligned} H_b(\boldsymbol{p}) = H_{SO} + \frac{1}{2\hbar^2 m_0}\big\{&4\hbar^2\gamma_2\boldsymbol{p}^2 + 2(\eta_1+2\eta_2)\boldsymbol{p}^2(\boldsymbol{I}\cdot\boldsymbol{S}_h) \\ &- 6\gamma_2\big(p_1^2\boldsymbol{I}_1^2 + \text{c.p.}\big) - 12\eta_2\big(p_1^2\boldsymbol{I}_1\boldsymbol{S}_{h1} + \text{c.p.}\big) \\ &- 12\gamma_3(\{p_1,p_2\}\{\boldsymbol{I}_1,\boldsymbol{I}_2\} + \text{c.p.}) \\ &- 12\eta_3(\{p_1,p_2\}(\boldsymbol{I}_1\boldsymbol{S}_{h2} + \boldsymbol{I}_2\boldsymbol{S}_{h1}) + \text{c.p.})\big\} \end{aligned} \quad (2)$$

and the central-cell corrections H_{CCC} discussed below in Sec. II C. Here we use center-of-mass coordinates [5,24],

$$\begin{aligned} \boldsymbol{r} &= \boldsymbol{r}_e - \boldsymbol{r}_h, \quad \boldsymbol{R} = \frac{m_h\boldsymbol{r}_h + m_e\boldsymbol{r}_e}{m_h + m_e}, \\ \boldsymbol{P} &= \hbar\boldsymbol{K} = \boldsymbol{p}_e + \boldsymbol{p}_h, \quad \boldsymbol{p} = \hbar\boldsymbol{k} = \frac{m_h\boldsymbol{p}_e - m_e\boldsymbol{p}_h}{m_h + m_e}, \end{aligned} \quad (3)$$

with $\boldsymbol{r}_e$ and $\boldsymbol{r}_h$ the electron and hole positions, and $\boldsymbol{p}_e$ and $\boldsymbol{p}_h$ their corresponding momenta. The center-of-mass momentum is set to $\boldsymbol{P} = 0$. We use the effective and free electron masses m_e and m_0, respectively, the symmetrized product $\{a,b\} = \frac{1}{2}(ab+ba)$, the Luttinger parameters γ_j and η_j, and $\gamma_1' = \gamma_1 + m_0/m_e$, E_g is the gap energy, ε the dielectric constant, and c.p. denotes cyclic permutation. The band structure Hamiltonian (2) necessitates the introduction of the hole spin $\boldsymbol{S}_h$ and the quasispin $\boldsymbol{I}$, the latter allowing for a convenient description of the degenerate Γ_5^+ valence bands. The spin-orbit coupling,

$$H_{SO} = \frac{2}{3}\Delta\left(1 + \frac{1}{\hbar^2}\boldsymbol{I}\cdot\boldsymbol{S}_h\right), \quad (4)$$

leads to an energetic splitting Δ of the valence bands into the higher lying Γ_7^+ bands associated with the yellow exciton series and the lower lying Γ_8^+ bands associated with the green exciton series. The material parameters of cuprous oxide used in our calculations are listed in Table I.

B. Complex-coordinate rotation

The green exciton states lie above the band gap of the yellow series and are coupled to the yellow continuum. Hence, they form quasibound resonances rather than bound states, even without considering the coupling to the phonons. For their description, we introduce complex energies, whose imaginary part is related to the finite linewidth as $\gamma = -2\,\mathrm{Im}\,E$. To compute these eigenenergies, we perform the complex-coordinate rotation $\boldsymbol{r} \to \boldsymbol{r}e^{i\theta}$ [11,29,30]. It is important to note that, under the complex-coordinate rotation, the Hamiltonian (1) becomes a non-Hermitian operator, and thus allows for complex-valued eigenenergies, as schematically illustrated in Fig. 1. Continuum states are rotated into the lower complex energy plane, revealing the resonances, which are *hidden* in a Hermitian eigenvalue problem. If the rotation angle θ is chosen appropriately, the resonance states become square integrable. For additional details we refer the reader to Refs. [10,12].

TABLE I. Material parameters of Cu_2O used in the calculations.

Energy gap	$E_g = 2.172\,08$ eV	[3]
Spin-orbit coupling	$\Delta = 0.131$ eV	[25]
Effective electron mass	$m_e = 0.99m_0$	[26]
Effective hole mass	$m_h = 0.58m_0$	[26]
Luttinger parameters	$\gamma_1 = 1.76$	[25]
	$\gamma_2 = 0.7532$	[25]
	$\gamma_3 = -0.3668$	[25]
	$\eta_1 = -0.020$	[25]
	$\eta_2 = -0.0037$	[25]
	$\eta_3 = -0.0337$	[25]
Exchange interaction	$J_0 = 0.792$ eV	[18]
Short distance correction	$V_0 = 0.539$ eV	[18]
Lattice constant	$a = 0.42696$ nm	[27]
Dielectric constants	$\varepsilon_{s1} = \varepsilon = 7.5$	[28]
	$\varepsilon_{b1} = \varepsilon_{s2} = 7.11$	[28]
	$\varepsilon_{b2} = 6.46$	[28]
Energy of Γ_4^--LO phonons	$\hbar\omega_{LO1} = 18.7$ meV	[22]
	$\hbar\omega_{LO2} = 87$ meV	[22]

C. Central-cell corrections

For a correct description of the even-parity exciton states, additional central-cell corrections [18]

$$H_{CCC} = V^H + V_d + H_{exch}, \quad (5)$$

in the Hamiltonian (1) are necessary. Here, the Haken potential

$$\begin{aligned} V^H = -\frac{e^2}{4\pi\epsilon_0 r}\Bigg[&\frac{1}{2\epsilon_1^*}(e^{-r/\rho_{h1}} + e^{-r/\rho_{e1}}) \\ &+ \frac{1}{2\epsilon_2^*}(e^{-r/\rho_{h2}} + e^{-r/\rho_{e2}})\Bigg] \end{aligned} \quad (6)$$

describes corrections to the dielectric constant for small exciton radii,

$$V_d = -V_0 V_{uc}\delta(\boldsymbol{r}) \quad (7)$$

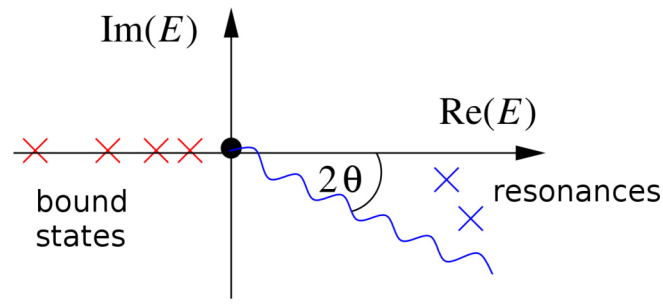

FIG. 1. Scheme of the complex-coordinate-rotation method. Resonances in the complex energy plane are hidden in Hermitian quantum mechanics but can be revealed by the complex-coordinate-rotation method. States representing the continuum are rotated into the complex plane by the angle 2θ around the respective threshold.

is an additional short distance correction [22], and

$$H_{\rm exch} = J_0\left(\frac{1}{4} - \frac{1}{\hbar^2}\boldsymbol{S}_{\rm e}\cdot\boldsymbol{S}_{\rm h}\right)V_{\rm uc}\delta(\boldsymbol{r}) \tag{8}$$

is the exchange interaction [20], which causes a splitting of the S-type states into ortho- and paraexcitons depending on the relative orientation of the electron and hole spins. For the central-cell corrections, we introduce the polaron radii

$$\rho_{{\rm e/h},i} = \sqrt{\frac{\hbar}{2m_{\rm e/h}\omega_{{\rm LO},i}}} \tag{9}$$

with the energies $\hbar\omega_{{\rm LO}i}$ of the longitudinal Γ_4^- phonons, and the values

$$\frac{1}{\epsilon_i^*} = \frac{1}{\epsilon_{{\rm b}i}} - \frac{1}{\epsilon_{si}}. \tag{10}$$

The parameters J_0 and V_0 are given in Table I; $V_{\rm uc} = a^3$ is the volume of the unit cell.

Due to the cubic crystal symmetry and the associated coupling to angular-momentum states with $\Delta l = \pm 2$, these corrections affect not only the S states but also the other even-parity states. The implementation of these terms requires the calculation of the complex-rotated matrix elements given in Appendix D of Ref. [18]. The difficulty is that these matrix elements form an alternating sum of terms with individually very large absolute values. Thus, an accurate calculation requires the use of a large number of significant digits. We therefore work with a computer algebra system to perform computations to arbitrary precision instead of standard double-precision calculations. With these preliminaries, we are now in the position to calculate the spectrum of even-parity green exciton states.

D. Non-Hermitian generalized eigenvalue problem

To calculate the eigenstates and eigenvalues of the Hamiltonian (1), we express the time-independent Schrödinger equation in a complete basis [5] using basis states

$$|\Pi\rangle = |N, L, (I, S_{\rm h})J, F, S_{\rm e}, F_{\rm t}, M_{F_{\rm t}}\rangle \tag{11}$$

with orbital angular momentum $\boldsymbol{L}$, effective hole spin $\boldsymbol{J}$ (as the sum of the quasispin $\boldsymbol{I}$ and the hole spin $\boldsymbol{S}_{\rm h}$), angular momentum $\boldsymbol{F} = \boldsymbol{J} + \boldsymbol{L}$, and total angular momentum $\boldsymbol{F}_{\rm t} = \boldsymbol{F} + \boldsymbol{S}_{\rm e}$ with its z component $M_{F_{\rm t}}$. Here, $\boldsymbol{S}_{\rm e}$ denotes the electron spin. For the radial part, we use complex rotated Coulomb-Sturmian functions [31],

$$U_{NL}(r) = N_{NL}(2r/\alpha)^L e^{-r/\alpha} L_N^{2L+1}(2r/\alpha), \tag{12}$$

which depend on L, and are additionally characterized by the radial quantum number N and the convergence parameter α. The latter can be used for the implementation of the complex scaling operation, allowing for the calculation of complex resonance states. To this end, a complex-valued $\alpha = |\alpha|e^{i\theta}$ is chosen, resulting in the complex rotation with angle θ.

When expressing the exciton states $|\Psi\rangle$ in the basis (11),

$$|\Psi\rangle = \sum_{\Pi} c_\Pi |\Pi\rangle, \tag{13}$$

the Schrödinger equation becomes a non-Hermitian generalized eigenvalue problem,

$$\boldsymbol{A}\boldsymbol{c} = E\boldsymbol{M}\boldsymbol{c} \tag{14}$$

with the Hamiltonian matrix $\boldsymbol{A}_{\Pi'\Pi} = \langle\Pi'|H|\Pi\rangle$, the overlap matrix $\boldsymbol{M}_{\Pi'\Pi} = \langle\Pi'|\Pi\rangle$, and the vector $\boldsymbol{c}$ containing the coefficients c_Π. Note that the overlap matrix $\boldsymbol{M}$ differs from the identity because the Coulomb-Sturmian functions (12) are not orthogonal. To obtain finite matrices and vectors, we introduce cut-offs to the quantum numbers $N + L + 1 \leqslant n_{\rm max}$ and $F \leqslant F_{\rm max}$. These parameters, together with $|\alpha|$ and θ have to be chosen appropriately to ensure properly converged results. Good convergence is reached when variations of the parameters do not lead to significant changes in the calculated spectra.

We first diagonalize the Hamiltonian excluding the singular Dirac delta terms V_d and $H_{\rm exch}$ of the central-cell corrections (5). From the high-dimensional matrices, we are only interested in a small window of eigenstates. For this aim an iterative method is implemented (e.g., in the ARPACK package [32]) that allows for the calculation of eigenvalues and eigenvectors near a controllable predetermined energy, which is numerically more efficient than a direct diagonalization.

After this, we set up a second eigenvalue problem where we include the delta terms with only the converged eigenstates from the first diagonalization. For this, we diagonalize the entire resulting low-dimensional eigenvalue problem using a direct LAPACK method [33].

III. DIPOLE TRANSITIONS BETWEEN EXCITONIC STATES

In the following, we investigate dipole transitions between different exciton states which is in contrast to earlier work that focused mostly on transitions from the crystal ground state [5,10,18]. The central quantity describing the transition from an initial exciton state $|\Psi_{\rm i}\rangle$ to the final exciton state $|\Psi_{\rm f}\rangle$ is the transition matrix element

$$M_{\rm fi} = \langle\Psi_{\rm f}|\hat{\boldsymbol{e}}_A\cdot\boldsymbol{\pi}|\Psi_{\rm i}\rangle \tag{15}$$

of the single-photon transition operator, with the polarization direction $\hat{\boldsymbol{e}}_A$ of the vector potential associated with the photon field

$$\boldsymbol{A}(\boldsymbol{x}) = \boldsymbol{A}_0 e^{i\boldsymbol{\kappa}\cdot\boldsymbol{x}} \approx \boldsymbol{A}_0 = A_0\hat{\boldsymbol{e}}_A \tag{16}$$

in dipole approximation, where we assume that the momentum $\hbar\kappa$ of the photon is much smaller than the relative momentum of exciton and hole. The operator

$$\boldsymbol{\pi} = m_0\boldsymbol{v} = m_0\frac{\partial\boldsymbol{x}}{\partial t} = \frac{im_0}{\hbar}[\mathcal{H}, \boldsymbol{x}] \tag{17}$$

denotes the kinetic momentum operator in a crystal with spin-orbit interaction, and appears during the minimal-substitution procedure. Note that it differs from the quasimomentum $\boldsymbol{p}$ associated with the Bloch eigenfunctions of the band Hamiltonian $\mathcal{H}$. The position operator $\boldsymbol{x}$ also has to be distinguished from the coordinates $\boldsymbol{r}_{\rm e}$ and $\boldsymbol{r}_{\rm h}$ that arise from the lattice positions in the continuum description of the crystal.

For the interseries transitions discussed in this paper, $|\Psi_{\rm i}\rangle$ is mostly a bound yellow exciton state and $|\Psi_{\rm f}\rangle$ is an unbound

green exciton resonance. It is therefore sufficient to consider the matrix elements in a basis, e.g., with the basis states (11); the transition amplitudes for the eigenstates can then be obtained by forming appropriate superpositions,

$$M_{\hat{\mathrm{fi}}} = \sum_{\Pi',\Pi} c^{\mathrm{f}}_{\Pi'} c^{\mathrm{i}}_{\Pi} \langle \Pi' | \hat{\boldsymbol{e}}_A \cdot \boldsymbol{\pi} | \Pi \rangle. \tag{18}$$

Note that the coefficients for the left (bra vector) basis states are not complex conjugated, since they would be real valued without the complex-coordinate rotation.

A. Operator identity between kinetic momentum and derivatives of the band Hamiltonian

We will now derive an operator identity between the kinetic momentum $\boldsymbol{\pi}$ and the derivatives of the band Hamiltonian $H(\boldsymbol{p})$ with respect to the momenta. For that, we consider arbitrary single exciton states, which are effective two-particle states of an electron with spin $\boldsymbol{S}_{\mathrm{e,z}} = \sigma_{\mathrm{e}}$ in the conduction band (c) and a hole with effective hole spin $\boldsymbol{J}_{\mathrm{h,z}} = \sigma_{\mathrm{h}}$ in the valence band (v). An excitonic state with center-of-mass momentum $\boldsymbol{P}$ can then be written as

$$\left|\Psi^{\mathrm{c,v}}_{\tau,\boldsymbol{P}}\right\rangle = \sum_{\boldsymbol{p}} \phi_{\tau,\boldsymbol{P}}(\boldsymbol{p})\, a^{\dagger}_{\mathrm{c},\sigma_{\mathrm{e}},\boldsymbol{p}+\alpha_{\mathrm{e}}\boldsymbol{P}}\, b^{\dagger}_{\mathrm{v},\sigma_{\mathrm{h}},-\boldsymbol{p}+\alpha_{\mathrm{h}}\boldsymbol{P}} |\Psi_0\rangle \tag{19}$$

where $\tau = \{N, L, M, \sigma_{\mathrm{e}}, \sigma_{\mathrm{h}}\}$ is a shorthand notation for all the additional quantum numbers of the exciton, $a^{\dagger}_{\mathrm{c},\sigma,\boldsymbol{q}}$ ($b^{\dagger}_{\mathrm{v},\sigma,\boldsymbol{q}}$) denotes an electron (hole) creation operator, and $|\Psi_0\rangle$ the crystal ground state. The coefficients α_{e} and α_{h} stem from the transformation from electron-hole coordinates to relative and center-of-mass coordinates. They are in principle arbitrary but must fulfill $\alpha_{\mathrm{e}} + \alpha_{\mathrm{h}} = 1$. We have chosen the same coefficients for all states.

1. Dipole approximation

In the dipole approximation, the excitonic center-of-mass momentum $\boldsymbol{P}$ vanishes and Eq. (19) reduces to

$$\left|\Psi^{\mathrm{c,v}}_{\tau}\right\rangle = \sum_{\boldsymbol{p}} \phi_{\tau}(\boldsymbol{p})\, a^{\dagger}_{\mathrm{c},\sigma_{\mathrm{e}},\boldsymbol{p}}\, b^{\dagger}_{\mathrm{v},\sigma_{\mathrm{h}},-\boldsymbol{p}} |\Psi_0\rangle. \tag{20}$$

The single-photon transition operator in dipole approximation, projected onto the Hilbert space spanned by the states in Eq. (20), can be written as

$$\frac{e\boldsymbol{A}_0\boldsymbol{\pi}}{m_0} \tag{21}$$

$$= \frac{e\boldsymbol{A}_0}{m_0} \sum_{\nu,\nu'} \sum_{\sigma_{\mathrm{e}},\sigma'_{\mathrm{e}}} \sum_{\boldsymbol{q}} \langle \nu, \sigma_{\mathrm{e}}, \boldsymbol{q} | \boldsymbol{\pi} | \nu', \sigma'_{\mathrm{e}}, \boldsymbol{q} \rangle\, a^{\dagger}_{\nu,\sigma_{\mathrm{e}},\boldsymbol{q}}\, a_{\nu',\sigma'_{\mathrm{e}},\boldsymbol{q}}$$

$$+ \frac{e\boldsymbol{A}_0}{m_0} \sum_{\xi,\xi'} \sum_{\sigma_{\mathrm{h}},\sigma'_{\mathrm{h}}} \sum_{\boldsymbol{q}} \langle \xi, \sigma_{\mathrm{h}}, \boldsymbol{q} | \boldsymbol{\pi} | \xi', \sigma'_{\mathrm{h}}, \boldsymbol{q} \rangle\, b^{\dagger}_{\xi,\sigma_{\mathrm{h}},\boldsymbol{q}}\, b_{\xi',\sigma'_{\mathrm{h}},\boldsymbol{q}}, \tag{22}$$

where $\boldsymbol{A}_0$ denotes the vector potential (16), the indices ν, ν' sum over all conduction bands, the indices ξ, ξ' sum over all valence bands, and the $\sigma_{\mathrm{e/h}}$ denote the corresponding substates (spins). In the derivation of Eq. (21), the Coulomb gauge has been used and the diamagnetic term was ignored, as it only has an appreciable influence for very high field strengths of the incoming electromagnetic wave. Upon evaluating a matrix element of the kind $e\boldsymbol{A}_0 \langle \Psi^{\mathrm{c,v}}_{\tau} | \boldsymbol{\pi} | \Psi^{\mathrm{c',v'}}_{\tau'} \rangle / m_0$, there are four cases that must be analyzed separately.

(i) Intraseries transitions: Here, we have $\{\mathrm{c}, \sigma_{\mathrm{e}}\} = \{\mathrm{c}', \sigma'_{\mathrm{e}}\}$ and $\{\mathrm{v}, \sigma_{\mathrm{h}}\} = \{\mathrm{v}', \sigma'_{\mathrm{h}}\}$. Applying the fermionic anticommutation rules for the creation and annihilation operators, one arrives at

$$\left\langle \Psi^{\mathrm{c,v}}_{\tau} \middle| \boldsymbol{\pi} \middle| \Psi^{\mathrm{c,v}}_{\tau'} \right\rangle = \sum_{\boldsymbol{p}} \phi_{\tau'}(\boldsymbol{p})\, \phi^{\dagger}_{\tau}(\boldsymbol{p}) (\langle \mathrm{c}, \sigma_{\mathrm{e}}, \boldsymbol{p} | \boldsymbol{\pi} | \mathrm{c}, \sigma_{\mathrm{e}}, \boldsymbol{p} \rangle + \langle \mathrm{v}, \sigma_{\mathrm{h}}, -\boldsymbol{p} | \boldsymbol{\pi} | \mathrm{v}, \sigma_{\mathrm{h}}, -\boldsymbol{p} \rangle). \tag{23}$$

(ii) Hole-driven interseries transitions: In this case, we have $\{\mathrm{c}, \sigma_{\mathrm{e}}\} = \{\mathrm{c}', \sigma'_{\mathrm{e}}\}$ but $\{\mathrm{v}, \sigma_{\mathrm{h}}\} \neq \{\mathrm{v}', \sigma'_{\mathrm{h}}\}$. Hence, we arrive at

$$\left\langle \Psi^{\mathrm{c,v}}_{\tau} \middle| \boldsymbol{\pi} \middle| \Psi^{\mathrm{c,v'}}_{\tau'} \right\rangle = \sum_{\boldsymbol{p}} \phi_{\tau'}(\boldsymbol{p})\, \phi^{\dagger}_{\tau}(\boldsymbol{p})\, \langle \mathrm{v}, \sigma_{\mathrm{h}}, -\boldsymbol{p} | \boldsymbol{\pi} | \mathrm{v}', \sigma'_{\mathrm{h}}, -\boldsymbol{p} \rangle. \tag{24}$$

(iii) Electron-driven interseries transitions: Here, we have $\{\mathrm{c}, \sigma_{\mathrm{e}}\} \neq \{\mathrm{c}', \sigma'_{\mathrm{e}}\}$ but $\{\mathrm{v}, \sigma_{\mathrm{h}}\} = \{\mathrm{v}', \sigma'_{\mathrm{h}}\}$. This case yields

$$\left\langle \Psi^{\mathrm{c,v}}_{\tau} \middle| \boldsymbol{\pi} \middle| \Psi^{\mathrm{c',v}}_{\tau'} \right\rangle = \sum_{\boldsymbol{p}} \phi_{\tau'}(\boldsymbol{p})\, \phi^{\dagger}_{\tau}(\boldsymbol{p})\, \langle \mathrm{c}, \sigma_{\mathrm{e}}, \boldsymbol{p} | \boldsymbol{\pi} | \mathrm{c}', \sigma'_{\mathrm{e}}, \boldsymbol{p} \rangle. \tag{25}$$

(iv) Two-particle transitions: In this case, one has $\{\mathrm{c}, \sigma_{\mathrm{e}}\} \neq \{\mathrm{c}', \sigma'_{\mathrm{e}}\}$ and $\{\mathrm{v}, \sigma_{\mathrm{h}}\} \neq \{\mathrm{v}', \sigma'_{\mathrm{h}}\}$. These transitions are forbidden to all orders in single-photon transitions and will not be discussed further.

The transitions from the yellow to the green series in Cu_2O are predominantly hole driven, although there might be an admixture of yellow states into the green series and vice versa.

2. Bloch matrix elements

The interband matrix elements $\langle n, \sigma, \boldsymbol{p} | \boldsymbol{\pi} | n', \sigma', \boldsymbol{p} \rangle$, which are expressed in terms of Bloch states, can be written in terms of the lattice periodic functions $|u_{n,\sigma}, \boldsymbol{p}\rangle$ via $|n, \sigma, \boldsymbol{p}\rangle = e^{(i/\hbar)\boldsymbol{p}\boldsymbol{r}} |u_{n,\sigma}, \boldsymbol{p}\rangle$ which results in

$$\langle n, \sigma, \boldsymbol{p} | \boldsymbol{\pi} | n', \sigma', \boldsymbol{p} \rangle = \langle u_{n,\sigma}, \boldsymbol{p} | \boldsymbol{\pi} | u_{n',\sigma'}, \boldsymbol{p} \rangle + \boldsymbol{p} \delta_{n n'}\, \delta_{\sigma \sigma'}. \tag{26}$$

Here n, n' denote the bands and σ, σ' the associated spins. The Hamiltonian acting on these lattice periodic functions is the $\boldsymbol{p} \cdot \boldsymbol{\pi}$ Hamiltonian (usually referred to as the $\boldsymbol{k} \cdot \boldsymbol{\pi}$ Hamiltonian with $\boldsymbol{k} = \boldsymbol{p}/\hbar$)

$$\mathcal{H}_{\boldsymbol{p}\cdot\boldsymbol{\pi}} = \mathcal{H}_0 + \mathcal{H}_{\boldsymbol{p}}, \tag{27}$$

with

$$\mathcal{H}_0 = -\frac{\hbar^2 \nabla^2}{2m_0} + V(\boldsymbol{x}) - \frac{i\hbar^2}{4m_0^2 c^2} [\boldsymbol{\sigma} \times \nabla V(\boldsymbol{x})] \cdot \nabla, \tag{28}$$

$$\mathcal{H}_{\boldsymbol{p}} = \frac{\boldsymbol{p}}{m_0} \cdot \boldsymbol{\pi} + \frac{\boldsymbol{p}^2}{2m_0}, \tag{29}$$

where $V(\boldsymbol{x})$ is the lattice periodic potential, $\boldsymbol{\sigma}$ the vector of Pauli matrices, and $\mathcal{H}_0$ denotes the Hamiltonian at the Γ point.

This implies the relation

$$\boldsymbol{\pi} = m_0 \boldsymbol{v} = m_0 \frac{\partial \mathcal{H}_{\boldsymbol{p}\cdot\boldsymbol{\pi}}}{\partial \boldsymbol{p}} - \boldsymbol{p}. \tag{30}$$

Inserting Eq. (30) into Eq. (26), we arrive at

$$\langle n, \sigma, \boldsymbol{p}|\boldsymbol{\pi}|n', \sigma', \boldsymbol{p}\rangle = m_0 \langle u_{n,\sigma}, \boldsymbol{p}| \frac{\partial \mathcal{H}_{\boldsymbol{p}\cdot\boldsymbol{\pi}}}{\partial \boldsymbol{p}} |u_{n',\sigma'}, \boldsymbol{p}\rangle. \tag{31}$$

A perturbation theoretical analysis of Eq. (31) up to first order in $\boldsymbol{p}$ has already been performed previously[16], yielding

$$\langle n, \sigma, \boldsymbol{p}|\boldsymbol{\pi}|n', \sigma', \boldsymbol{p}\rangle = m_0 \langle u_{n,\sigma}, 0| \frac{\partial \mathcal{H}_{\boldsymbol{p}\cdot\boldsymbol{\pi}}}{\partial \boldsymbol{p}} |u_{n',\sigma'}, 0\rangle. \tag{32}$$

The $\boldsymbol{p}\cdot\boldsymbol{\pi}$ Hamiltonian $\mathcal{H}_{\boldsymbol{p}\cdot\boldsymbol{\pi}}$ describes the $\boldsymbol{p}$-dependent band dispersion in the crystal. In our system, this is identified with the kinetic energies of the electron in the conduction band H_c and hole in the valence band H_v, respectively. Using the kinetic part of the Hamiltonian (1),

$$T(\boldsymbol{p}) = H_\mathrm{c}(\boldsymbol{p}) - H_\mathrm{v}(\boldsymbol{p}) = \frac{\gamma_1'}{2m_0}\boldsymbol{p}^2 + H_\mathrm{b}(\boldsymbol{p}), \tag{33}$$

we can summarize all three cases in Eqs. (23)–(25) via

$$\begin{aligned}
&\left\langle \Psi_\tau^{\mathrm{c,v}} | \boldsymbol{\pi} | \Psi_{\tau'}^{\mathrm{c,v}'} \right\rangle \\
&\quad = m_0 \sum_{\boldsymbol{p}} \phi_\tau^\dagger(\boldsymbol{p}) \phi_{\tau'}(\boldsymbol{p}) \langle \mathrm{c}, \sigma_\mathrm{e}, \mathrm{v}, \sigma_\mathrm{h} | \partial_{\boldsymbol{p}} T(\boldsymbol{p}) | \mathrm{c}, \sigma_\mathrm{e}', \mathrm{v}', \sigma_\mathrm{h}' \rangle \\
&\quad = m_0 \int d^3\boldsymbol{r}\, \psi_\tau^\dagger(\boldsymbol{r}) \underbrace{\langle \mathrm{c}, \sigma_\mathrm{e}, \mathrm{v}, \sigma_\mathrm{h} | \partial_{\boldsymbol{p}} T(\boldsymbol{p}) | \mathrm{c}, \sigma_\mathrm{e}', \mathrm{v}', \sigma_\mathrm{h}' \rangle}_{\mathcal{O}(\boldsymbol{p})} \psi_{\tau'}(\boldsymbol{r}),
\end{aligned} \tag{34}$$

where the matrix element is evaluated in the 12-dimensional basis of electron-hole spin states $|\mathrm{c}, \sigma_\mathrm{e}, \mathrm{v}, \sigma_\mathrm{h}\rangle$. The second line gives the equivalent expression in real space, where $\psi_\tau(\boldsymbol{r})$ is the real-space envelope function of the state $|\Psi_{\tau'}^{\mathrm{c,v}'}\rangle$. These states span the same Hilbert space as the basis states (11). Noting that only the kinetic energy terms in the Hamiltonian (1) contain the relative momentum operator $\boldsymbol{p}$, we obtain the identity

$$\boldsymbol{\pi} = m_0 \frac{\partial}{\partial \boldsymbol{p}} H(\boldsymbol{p}) \tag{35}$$

valid for the one-exciton states considered in this paper. Equation (35) is an operator identity in the one-exciton Hilbert space spanned, e.g., by the basis (11), and is valid for vanishing center-of-mass momentum $\boldsymbol{P}$ and relative momentum $\boldsymbol{p}$ much smaller than the extent of the Brillouin zone.

B. Numerical evaluation of the matrix elements $\langle \Pi' | \pi_z | \Pi \rangle$

The computation of the dipole transition matrix elements M_fi in Eq. (18) requires one to evaluate the matrix elements $\langle \Pi' | \boldsymbol{\pi} | \Pi \rangle$ of the operator (35) in the basis (11).

From Eq. (35) we obtain

$$\frac{\boldsymbol{\pi}}{m_0} = \frac{\partial}{\partial \boldsymbol{p}} H(\boldsymbol{p}) = \frac{\gamma_1' \boldsymbol{p}}{m_0} + \frac{\partial H_\mathrm{b}(\boldsymbol{p})}{\partial \boldsymbol{p}}. \tag{36}$$

We focus on the component π_z for light polarized along the z axis. The matrix elements for p_z in the basis (11) are derived in Appendix A. The more difficult part is to evaluate the second term in Eq. (36). Instead of deriving the expression in detail here, we connect this problem to terms already calculated in Ref. [34]. They consider the Hamiltonian (1) in center-of-mass coordinates with a nonvanishing center-of-mass momentum $P = \hbar K$ parallel to a given axis. Here, we are interested in the case $\boldsymbol{P} \parallel [001]$ related to the derivative with respect to p_z. This means that we can set $\boldsymbol{P} = P\boldsymbol{e}_z$ in the following. Following Ref. [34], we expand the Hamiltonian in powers of P as

$$H(\boldsymbol{p}, \boldsymbol{P}) = H_0 + PH_1 + P^2 H_2. \tag{37}$$

The center-of-mass transformation (3) is chosen in such a way that terms linear in $\boldsymbol{P}$ vanish without the corrections from the valence band. This means that the term H_1 arises solely from the kinetic energy H_h of the hole. More explicitly, we can write

$$\begin{aligned}
&H_\mathrm{h}(\boldsymbol{p}_\mathrm{h} = -\boldsymbol{p} + \alpha_\mathrm{h}\boldsymbol{P}) \\
&\qquad = \frac{\boldsymbol{p}^2}{2m_\mathrm{h}} + H_\mathrm{b}(\boldsymbol{p}) - \frac{\alpha_\mathrm{h} P}{m_\mathrm{h}} p_z + PH_1 + O(P^2),
\end{aligned} \tag{38}$$

where $\alpha_\mathrm{h} = m_\mathrm{h}/(m_\mathrm{h} + m_\mathrm{e})$ is determined by the center-of-mass transformation. We first differentiate both sides with respect to $P = P_z$ and evaluate at $P = 0$,

$$\alpha_\mathrm{h} \frac{\partial H_\mathrm{h}}{\partial p_{\mathrm{h},z}}(\boldsymbol{p}_\mathrm{h} = -\boldsymbol{p}) = -\alpha_\mathrm{h} \frac{\partial H_\mathrm{h}}{\partial p_z}(-\boldsymbol{p}) = -\frac{\alpha_\mathrm{h}}{m_\mathrm{h}} p_z + H_1. \tag{39}$$

On the other hand, first setting $P = 0$ and differentiating with respect to p_z leads to

$$\frac{\partial H_\mathrm{h}}{\partial p_z}(-\boldsymbol{p}) = \frac{p_z}{m_\mathrm{h}} + \frac{\partial H_\mathrm{b}(\boldsymbol{p})}{\partial p_z}. \tag{40}$$

Comparing these results, we obtain the identity

$$\frac{\partial H_\mathrm{b}}{\partial p_z}(\boldsymbol{p}) = -\frac{1}{\alpha_\mathrm{h}} H_1 = -\frac{m_\mathrm{e}\gamma_1'}{m_0} H_1. \tag{41}$$

Inserted into Eq. (36), we finally find

$$\pi_z = \gamma_1'(p_z - m_\mathrm{e} H_1), \tag{42}$$

with [34]

$$\begin{aligned}
H_1 = &-\frac{1}{2\hbar^2 m_\mathrm{e}} \left\{ 2\sqrt{\frac{5}{3}} \mu' [P^{(1)} \times I^{(2)}]_0^{(1)} \right. \\
&\left. + 4\sqrt{\frac{2}{5}} \delta' [P^{(1)} \times I^{(2)}]_0^{(3)} \right\} \\
&- \frac{3\eta_1}{\gamma_1' \hbar^2 m_\mathrm{e}} \left\{ \frac{2}{3} P_0^{(1)} \left(I^{(1)} \cdot S_\mathrm{h}^{(1)} \right) + 2\sqrt{\frac{5}{3}} \nu [P^{(1)} \times D^{(2)}]_0^{(1)} \right. \\
&\left. + 4\sqrt{\frac{2}{5}} \tau [P^{(1)} \times D^{(2)}]_0^{(3)} \right\},
\end{aligned} \tag{43}$$

using the abbreviations

$$D_k^{(2)} = \left[I^{(1)} \times S_\mathrm{h}^{(1)} \right]_k^{(2)} \tag{44}$$

and

$$\mu' = \frac{6\gamma_3 + 4\gamma_2}{5\gamma_1'}, \quad \delta' = \frac{\gamma_3 - \gamma_2}{\gamma_1'},$$
$$\nu = \frac{6\eta_3 + 4\eta_2}{5\eta_1}, \quad \tau = \frac{\eta_3 - \eta_2}{\eta_1}. \tag{45}$$

All relevant matrix elements can be found in Ref. [34].

IV. RESULTS AND DISCUSSION

In the following, we present our results for the dipole transition probabilities for two cases of interseries transitions. As parity is an exact quantum number, we separately discuss transitions first from odd-parity to even-parity states, and then from even-parity to odd-parity states. We choose a coordinate system where the x, y, and z axes are parallel to the [100], [010], and [001] directions, respectively.

A. Interseries absorption spectra

The transition matrix elements M_{fi} can be used to calculate interseries absorption spectra. The photoabsorption cross section σ_{i} from the initial state $|\Psi_{\mathrm{i}}\rangle$ at the spectral position $E = \hbar\omega_{\mathrm{ph}}$ is given by [12,35]

$$\sigma_{\mathrm{i}}(\omega_{\mathrm{ph}}) = \frac{4\pi\alpha\hbar}{m_0^2\omega_{\mathrm{ph}}}\mathrm{Im}\sum_{\mathrm{f}}\frac{M_{\mathrm{fi}}M_{\mathrm{if}}}{E_{\mathrm{f}} - E_{\mathrm{i}} - \hbar\omega_{\mathrm{ph}}}, \tag{46}$$

with the fine-structure constant α and $\hbar\omega_{\mathrm{ph}} \approx E_{\mathrm{f}} - E_{\mathrm{i}}$. Note that in general, $M_{\mathrm{fi}} \neq M_{\mathrm{if}}^*$ for complex rotated states, and thus the numerator in Eq. (46) does not simplify to $|M_{\mathrm{fi}}|^2$.

To avoid extremely narrow peaks for certain states, we phenomenologically model an additional linewidth caused by the coupling to phonons in the crystal. In a simplified model, the phonon-induced linewidth has a power-law dependency on the principal quantum number n as [3,36]

$$\gamma_{\mathrm{ph}}(n) = \gamma_0^{\mathrm{ph}} n^{-3}. \tag{47}$$

We estimate the parameter $\gamma_0^{\mathrm{ph}} = 56.4$ meV and assign to each resonance an effective quantum number n_{eff} based on the real part of its energy as outlined in Appendix B. The resulting linewidth shifts the imaginary part of the complex energy according to $E_{\mathrm{f}} \rightarrow E_{\mathrm{f}} - i\gamma_{\mathrm{ph}}/2$.

B. Transitions from odd-parity yellow exciton states to even-parity green states

Experimentally, the most easily accessible yellow exciton states are the odd-parity Γ_4^- P states. As the interseries dipole transition flips the parity, the coupled states will be green even-parity states with S- and D-type envelopes. We now investigate two different scenarios. In the first, we select for the initial state the yellow P exciton transforming like the basis state z of the irreducible representation $\Gamma_4{}^-$ [37]. In the second scenario, we investigate the yellow P-exciton state transforming like the basis state y. In both cases, the photon polarization is along the z direction. From the product of the representations [37] $\Gamma_4^- \otimes \Gamma_4^- = \Gamma_1^+ + \Gamma_3^+ + \Gamma_4^+ + \Gamma_5^+$ we can determine which transitions to green states are allowed in principle.

TABLE II. Real (R) and imaginary (I) parts of squared transition matrix elements $M^2 = M_{\mathrm{if}}M_{\mathrm{fi}}$ in units of 10^{-6} $\mathrm{h}^2\,\mathrm{a_g^{-2}}$ for certain selected green exciton states of energy $E = \mathrm{Re}\,E_{\mathrm{f}}$. The initial odd parity yellow P state of irreducible representation Γ_4^- transforms like z and the light is polarized along the z direction.

	$2P$		$3P$		$4P$		$5P$	
E (eV)	R M^2	I M^2	R M^2	I M^2	R M^2	I M^2	R M^2	I M^2
2.28456	15.02	−19.56	−1.36	1.11	0.11	−1.55	0.32	−0.71
2.28583	22.59	−0.60	3.92	−0.12	0.66	−0.03	0.23	−0.01
2.28895	366.60	1.17	15.29	0.41	0.17	0.03	0.00	0.00
2.28949	41.06	1.24	2.22	0.10	0.03	0.01	0.00	0.00
2.29283	3.00	7.36	13.42	−10.83	2.20	−2.18	1.87	−0.88
2.29367	43.45	−0.67	1.61	−0.11	1.25	−0.05	0.47	−0.02
2.29439	180.87	1.34	8.95	1.14	9.62	0.29	0.85	0.06
2.29494	46.04	−0.51	139.46	0.42	26.58	0.50	3.05	0.15
2.29522	0.82	0.08	16.55	0.80	3.92	0.09	0.34	0.03
2.29710	9.91	−0.04	30.51	−0.08	0.03	0.02	1.32	0.06
2.29776	19.31	−0.29	12.41	−0.22	62.81	−0.05	29.01	0.28
2.29845	33.28	0.18	9.36	0.55	21.16	−0.69	8.31	0.52
2.29864	16.24	0.73	1.87	0.02	4.49	−0.43	0.20	0.10
2.29932	10.08	−0.18	6.92	−0.11	2.06	−0.08	25.78	−0.20

We begin with the yellow P exciton and the photon both transforming according to the z component of the Γ_4^- representation. This initial state can itself be excited using a one-photon absorption process with light polarized along the z direction. Using the tables in Ref. [37], we can deduce that the corresponding green states transform according to Γ_1^+ and the ψ_1^{3+} component of Γ_3^+. In Fig. 2, we show interseries transition spectra in this configuration. We additionally list the results for a selection of states in Table II.

Using the Rydberg energies of the yellow and green exciton series, we can estimate which green principal quantum number belongs to states with maximum overlap with a yellow exciton state with given principal quantum number. In the following, we use the values $E_{\mathrm{Ryd}}^{\mathrm{y}} = 86.04$ meV [23] and $E_{\mathrm{Ryd}}^{\mathrm{g}} = 150.4$ meV [10]. The Bohr radii a_0^{y} and a_0^{g} are related to the Rydberg energies by

$$\frac{a_0^{\mathrm{g}}}{a_0^{\mathrm{y}}} \approx \frac{E_{\mathrm{Ryd}}^{\mathrm{y}}}{E_{\mathrm{Ryd}}^{\mathrm{g}}}. \tag{48}$$

From a simple overlap argument, one would expect the transition strengths to be largest when the initial and final states have comparable real-space extensions. As the linear extension of the excitons scales with the square of the principal quantum number n, we derive the estimate

$$n_{\mathrm{g}} = \sqrt{\frac{E_{\mathrm{Ryd}}^{\mathrm{g}}}{E_{\mathrm{Ryd}}^{\mathrm{y}}}}n_{\mathrm{y}} \approx 1.32 n_{\mathrm{y}}, \tag{49}$$

to which the spectra in Figs. 2–5 fit approximately.

The resulting transition strengths are of the same order of magnitude as those found in Ref. [16]. The strongest transition in Table II is from the $2P$ yellow exciton to the exciton state with energy $E = 2.288\,95$ eV, which is a $3D$ state. The matrix elements become progressively weaker as the principal quantum number of the initial yellow state increases. At the same

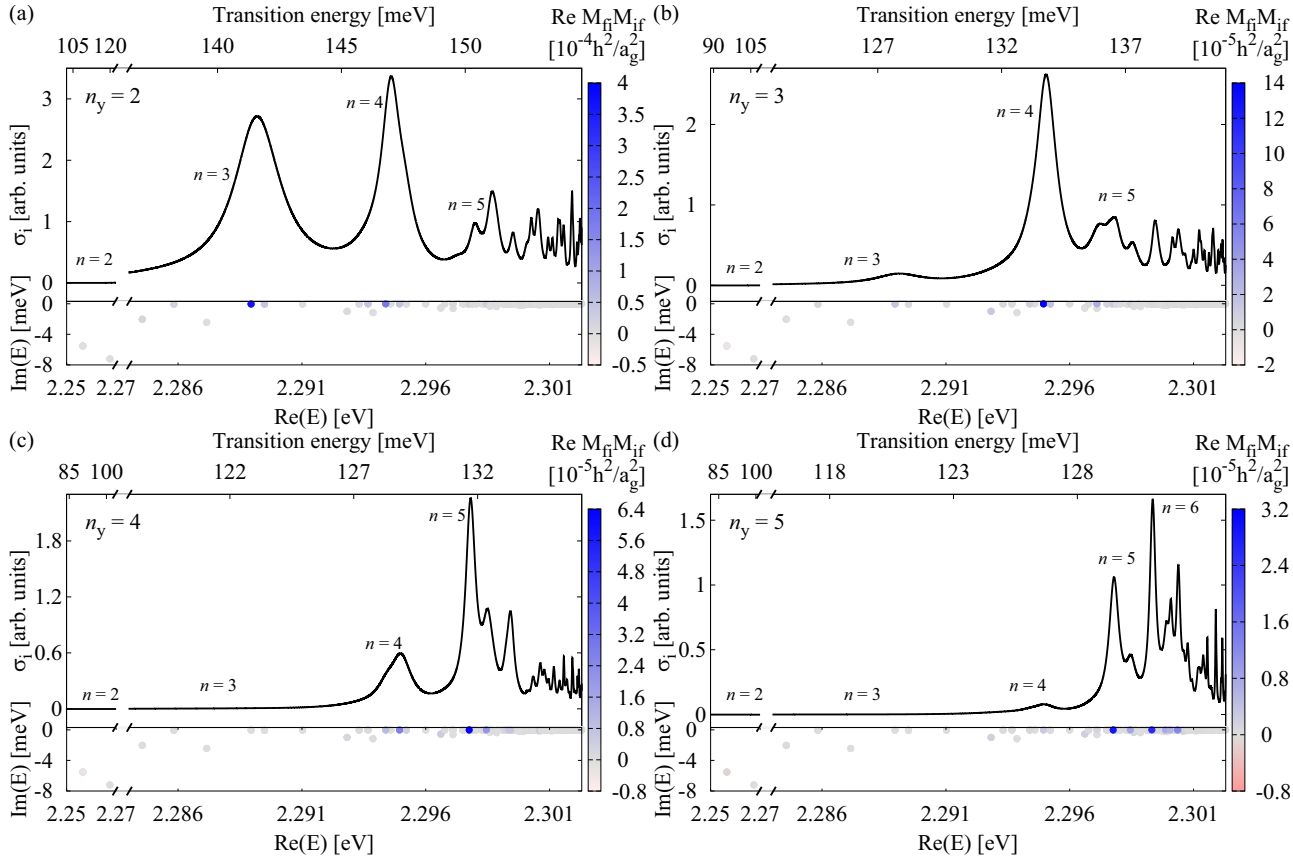

FIG. 2. Spectrum of transitions between odd-parity yellow P excitons transforming like the function z and even-parity green states. The transition is mediated by photons polarized in the z direction. In the top part of the panels, we show the spectrum using the linewidths derived from the complex rotation corrected by Eq. (47) to incorporate the influence of the phonons. The uncorrected complex energy is presented in the bottom part of the panel. The color additionally shows the real part of the square $M_{fi}M_{if}$ of the interseries transitions matrix element introduced in Eq. (15), which is proportional to the complex generalization of the oscillator strength.

time, with increasing principal quantum number of the initial state, the green states with the highest transition strengths move to higher energies, in accordance with Eq. (49).

Here, as well as in the following discussions, it is also important to remember that the choice of initial state not only influences the strength of the transition, but also the energy gap between the states. This is most evident in the configuration in Sec. IV C, where the initial state is of even parity, leading to differences in the transition energies of up to 100 meV.

We now proceed to the scenario that the P exciton transforms according to the Γ_4^- function y, meaning that the initial state can be excited using a single-photon absorption process with light polarized along the y direction. Here, the corresponding green excitons transform like the x component of Γ_4^+ and the xz component of Γ_5^+ [37]. In Fig. 3 we show a transition spectrum in this configuration. We additionally list the results for a selection of states in Table III.

The strongest transition in Table III is from the $2P$ yellow exciton to the exciton state with energy $E = 2.256\ 55$ eV, which is the lowest lying $2S$ state. Nevertheless, it is hardly visible in our simulated spectrum in Fig. 3 because of its much larger width as compared with the other states.

As the principal quantum number of the initial yellow state increases, the matrix elements here also become progressively weaker. The region of green states with the strongest transition from a given yellow state does not obey Eq. (49) as accurately as in the previous case, lying slightly lower energetically as expected. This could be related to the different spatial extensions of the addressed green states, in addition to the generally approximate character of the overlap argument.

C. Transitions from even-parity yellow states to odd-parity green states

We finally investigate transitions from yellow even-parity states to green odd-parity states. The former can be excited using two-photon absorption processes. For these transitions, we have to consider states with irreducible representations appearing in the tensor product $\Gamma_5^+ \otimes \Gamma_4^- = \Gamma_2^- + \Gamma_3^- + \Gamma_4^- + \Gamma_5^-$. In Fig. 4, we show spectra for transitions of this kind. As initial states, we chose excitons transforming according to the xy component of the irreducible representation Γ_5^+. In Table IV we list the results for a selection of states. In Fig. 5, we additionally show the special case of the transitions where the initial state is the *green* $1S$ state, which is energetically placed among the yellow excitons.

The strongest transition in Table IV is from the $2S$ yellow exciton to the green $2P$ exciton state with energy $E = 2.285\ 15$ eV. This is also the strongest transition we found

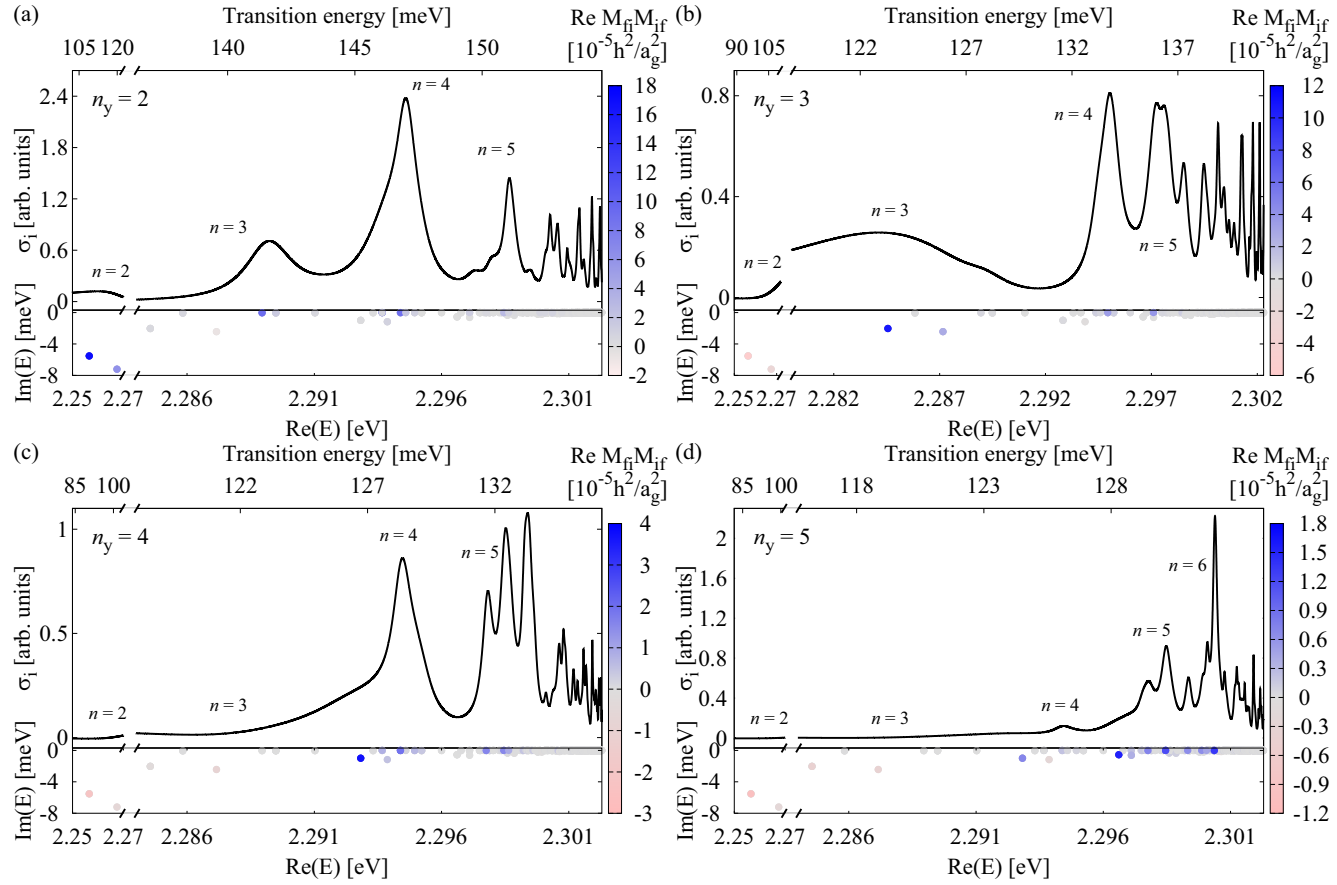

FIG. 3. Same as Fig. 2, but the initial odd-parity yellow P states transform like the function y.

among all configurations. This has to be balanced against the fact that the initial state is of even parity, which makes it inaccessible in one-photon transitions; it can, however, be excited using two-photon absorption.

We also investigated transitions from the $3D$ state [see panel (d) in Fig. 4]. These seem to be substantially stronger than the transitions from the $3S$ states, but still weaker than those from the $1S$ and $2S$ excitons. Finally, there are several

TABLE III. Same as Table II but the initial odd-parity yellow P states transform like y.

	$2P$		$3P$		$4P$		$5P$	
E (eV)	R M^2	I M^2	R M^2	I M^2	R M^2	I M^2	R M^2	I M^2
2.25655	170.05	295.75	−55.84	−10.02	−22.11	−16.43	−10.17	−10.68
2.26745	61.88	149.44	−24.63	−32.42	−5.93	−15.23	−2.25	−7.71
2.28456	4.52	13.21	107.45	70.38	−2.65	18.35	−4.21	5.47
2.28716	−7.42	6.12	27.30	44.18	−9.08	1.49	−3.92	−1.10
2.28895	91.65	0.29	3.82	0.10	0.04	0.01	0.00	0.00
2.29283	1.98	2.69	2.46	1.01	37.11	14.39	7.05	9.05
2.29367	116.25	0.95	1.11	−0.06	8.16	−0.21	1.67	−0.03
2.29439	9.83	−0.06	2.46	−0.17	18.61	−1.63	2.42	−0.03
2.29439	89.72	3.11	7.48	0.58	19.32	−1.38	2.23	0.04
2.29494	11.51	−0.13	34.86	0.11	6.64	0.12	0.76	0.04
2.29661	−0.59	0.36	−0.07	0.23	−0.27	−0.12	15.41	−2.43
2.29710	13.46	0.16	38.08	0.20	0.24	0.00	2.30	0.21
2.29776	4.83	−0.07	3.10	−0.06	15.70	−0.01	7.25	0.07
2.29845	11.70	0.75	3.82	0.27	4.92	−0.06	9.73	0.70
2.29845	28.58	1.00	8.52	0.61	15.28	−0.49	11.81	0.46
2.30037	8.11	0.23	2.82	0.29	0.19	−0.13	13.45	−1.78

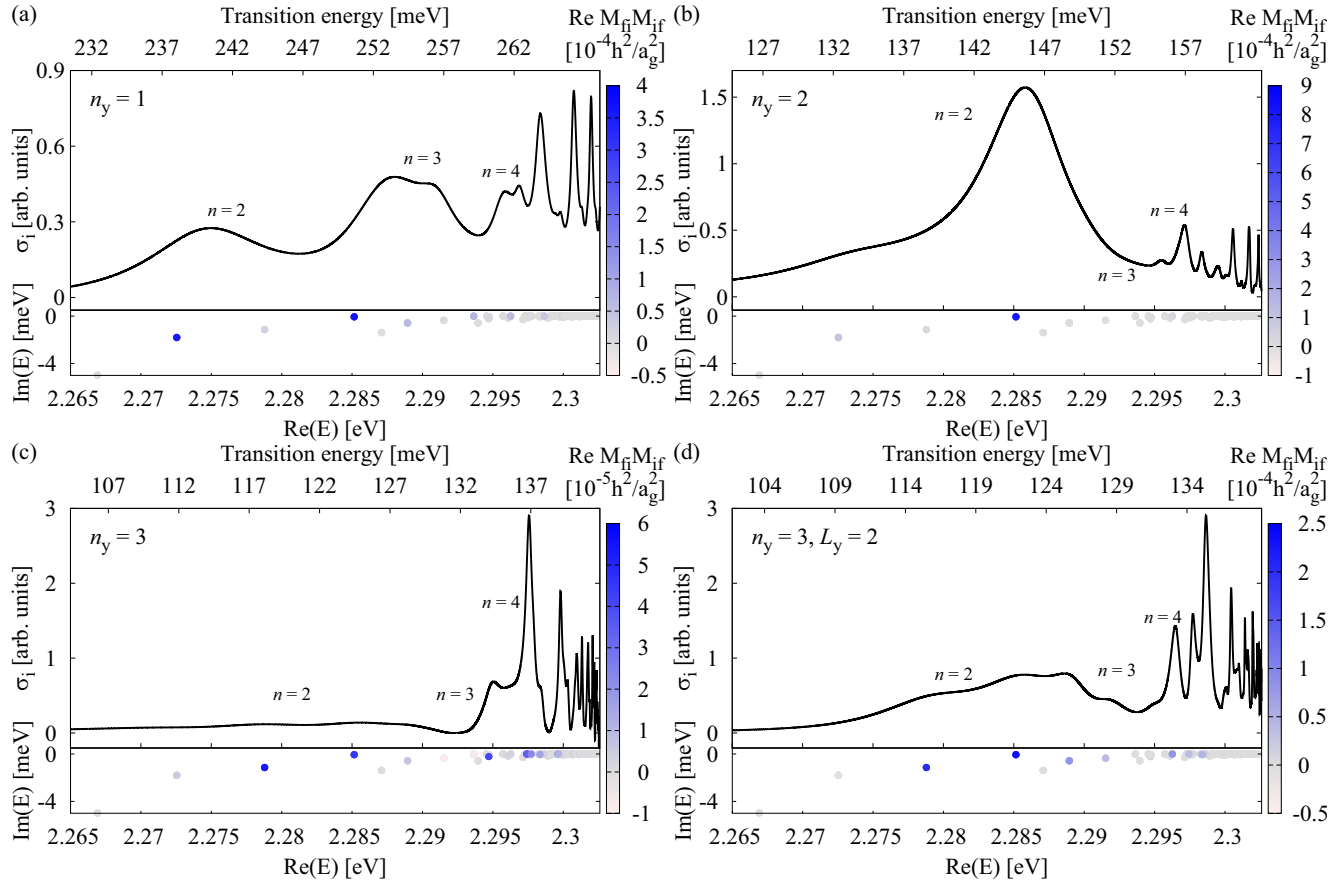

FIG. 4. Same as Fig. 2, but the initial even-parity states are S (a)–(c) and D (d) states transforming like the function xy of the irreducible representation Γ_5^+.

strong transitions starting from the green 1S exciton, but they are weaker than those from yellow 1S and 2S states.

V. CONCLUSION AND OUTLOOK

In this paper, we have investigated interseries transitions between the yellow and green exciton series in the dipole approximation. We extended the calculations for the yellow-to-green interseries transitions performed in Ref. [16] by including the complex valence-band structure. To properly take into account the associated coupling between the green exciton states and the yellow continuum, we used the complex-coordinate rotation method for the calculation of the green exciton resonances as described in Ref. [10].

We considered different choices for the initial state in the spectral range of the yellow series, concentrating mostly on the odd-parity P states, which are most easily accessible in one-photon absorption experiments. We distinguished the cases where the photon that excites the initial exciton is polarized parallel to the photon affecting the interseries transition from the scenario in which they are orthogonally polarized. Additionally, we also calculated the probabilities for the transition from the even-parity yellow states to the odd-parity green states, with the special case where the initial state is the *green* 1S exciton.

The transition strengths are on the same order of magnitude in the different configurations, with those starting at an odd-parity yellow exciton being somewhat weaker than

TABLE IV. Same as Table II but the initial even-parity yellow states transform like xy of the irreducible representation Γ_5^+. In the last two columns we show the transition matrix elements for the initial *green* 1S exciton state.

	1S		2S		3S		3D		1Sg	
E (eV)	R M^2	I M^2	R M^2	I M^2	R M^2	I M^2	R M^2	I M^2	R M^2	I M^2
2.27254	359.83	−18.09	96.55	−2.35	5.32	25.33	−6.76	−4.18	281.54	−48.83
2.27879	18.62	−0.17	14.24	26.43	53.84	18.82	200.93	−8.84	−22.05	11.59
2.28515	361.22	−121.21	801.02	151.17	45.41	−5.92	233.21	−6.17	350.48	−12.96
2.28894	65.09	−1.59	9.20	−0.18	6.69	1.34	82.51	29.60	108.16	−36.54
2.29364	71.87	−17.59	0.23	3.86	−7.84	−17.52	−2.82	−3.83	321.79	49.94
2.29626	61.26	−17.17	29.89	10.64	2.74	0.75	81.79	10.45	88.85	−9.54

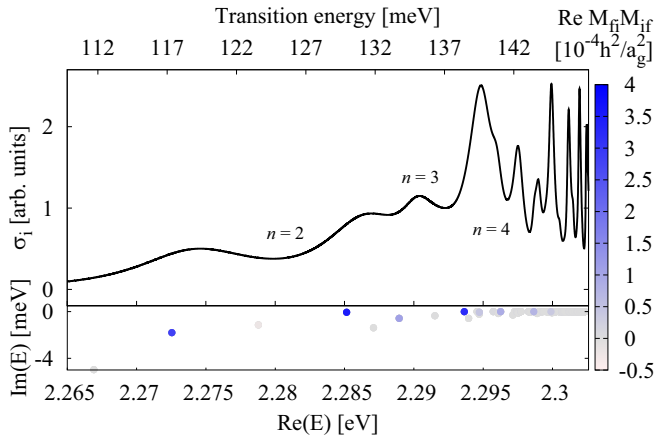

FIG. 5. Same as Fig. 4, but for the initial even-parity green $1S\ \Gamma_5^+$ exciton state transforming as xy.

those starting at an even-parity yellow exciton. Of course, the experimental preparation of the latter is more difficult, as a two-photon excitation is required. In all cases, increasing the principal quantum number of the initial state shifts the range of excited green states to higher energies, with an overall weakening of the transition strengths in most cases.

In this work, we use the dipole approximation, which is valid if the wavelength of the light affecting the interseries transition is much larger than the extension of the involved excitons. As shown in Ref. [16], this condition breaks down for transitions between the yellow and green series starting at $n \gtrsim 15$ for counterpropagating pump and probe beams. Extending our investigations to this parameter range thus requires going beyond the dipole approximation. Furthermore, an extension of our method to cover transitions between states of the yellow and blue series is relatively straightforward, but requires the implementation of the conduction band Hamiltonian including the Γ_8^- band. Another possible route is to investigate the influence of an additional external field to fine-tune the properties of the transitions.

Finally, one of the aims of our paper was to provide theoretical predictions which can help guide experimental investigations into the interseries transitions. While there has been some experimental work with respect to intraseries transitions within the yellow series [38,39] and with respect to interseries transitions between the yellow and blue series [40], here we have investigated the yellow-to-green interseries transitions. A comparison of our results with future experimental data is thus highly desirable.

ACKNOWLEDGMENTS

This work was supported by Deutsche Forschungsgemeinschaft (DFG) through Grant No. MA1639/13-1 and through Grant No. SCHE612/4-2 of the SPP 1929 "Giant Interactions in Rydberg Systems."

APPENDIX A: THE MATRIX ELEMENT FOR p_z

In the formalism of irreducible tensors, p_z is given by

$$p_z = P_0^{(1)}. \tag{A1}$$

In the Supplemental Material of Ref. [34], Eq. (14) provides the matrix elements for the operator

$$P_0^{(1)}\big(I^{(1)} \cdot S_h^{(1)}\big), \tag{A2}$$

which we can use here. Using the identity

$$I^{(1)} \cdot S_h^{(1)} = \frac{1}{2}\big(\boldsymbol{J}^2 - \boldsymbol{I}^2 - \boldsymbol{S}_h^2\big) = \frac{2J(2J+2) - 11}{8}, \tag{A3}$$

we can calculate the matrix element for p_z using

$$\langle \Pi' | P_0^{(1)} | \Pi \rangle = \frac{8}{2J(2J+2) - 11} \langle \Pi' | P_0^{(1)} \big(I^{(1)} \cdot S_h^{(1)}\big) | \Pi \rangle. \tag{A4}$$

Here, $|\Pi\rangle$ and $|\Pi'\rangle$ denote basis states as given in Eq. (11).

APPENDIX B: PHONON-INDUCED LINEWIDTHS

In order to use Eq. (47), we need to determine the constant γ_0^{ph}. According to Ref. [7], the FWHM of the green $2P$ state at $T = 4$ K is $\gamma^{2P} = 17.7$ meV. In Ref. [10], the complex coordinate rotation method was used to calculate the complex energies of the odd-parity green excitons, and to determine the linewidths γ_{cont} caused by the coupling of the green excitons to the yellow continuum. Here, we update this calculation by adding the Haken potential to the Hamiltonian, and find $\gamma_{\mathrm{cont}}^{2P} = 9.95$ meV for the green $2P$ state. We can thus estimate the phonon-induced linewidth of the $2P$ green exciton as

$$\begin{aligned}\gamma_{\mathrm{ph}}(n=2) &= \gamma^{2P} - \gamma_{\mathrm{cont}}^{2P} \\ &\approx 17.7\ \mathrm{meV} - 9.95\ \mathrm{meV} = 7.05\ \mathrm{meV}\end{aligned} \tag{B1}$$

leading to

$$\gamma_0^{\mathrm{ph}} = 8 \times \gamma_{\mathrm{ph}}(n=2) = 8 \times 7.05\ \mathrm{meV} = 56.4\ \mathrm{meV}. \tag{B2}$$

We associate to each resonance an effective quantum number n_{eff} as a function of the real part of the resonance energy E,

$$n_{\mathrm{eff}} = \sqrt{\frac{E_{\mathrm{Ryd}}}{E_{\mathrm{gap}} - E}} + \delta. \tag{B3}$$

The values $E_{\mathrm{Ryd}} = 142$ meV, $E_{\mathrm{gap}} = 2.302\,92$ eV, and $\delta = 0.1$ were obtained by a phenomenological fit to the odd-parity green excitons in an updated version of the calculation in Ref. [10], where we included the Haken potential. Note that these values should not be taken as the literal Rydberg energy and quantum defect, as the inclusion of the Haken potential distorts the Rydberg spectrum.

[1] E. F. Gross and N. A. Karryev, Opticheskii spektr eksitona, Dokl. Akad. Nauk SSSR **84**, 471 (1952).

[2] E. F. Gross, Optical spectrum of excitons in the crystal lattice, Il Nuovo Cimento (1955-1965) **3**, 672 (1956).

[3] T. Kazimierczuk, D. Fröhlich, S. Scheel, H. Stolz, and M. Bayer, Giant Rydberg excitons in the copper oxide Cu_2O, Nature (London) **514**, 343 (2014).

[4] J. Thewes, J. Heckötter, T. Kazimierczuk, M. Aßmann, D. Fröhlich, M. Bayer, M. A. Semina, and M. M. Glazov, Observation of High Angular Momentum Excitons in Cuprous Oxide, Phys. Rev. Lett. **115**, 027402 (2015).

[5] F. Schweiner, J. Main, M. Feldmaier, G. Wunner, and C. Uihlein, Impact of the valence band structure of Cu_2O on excitonic spectra, Phys. Rev. B **93**, 195203 (2016).

[6] R. J. Elliott, Symmetry of Excitons in Cu_2O, Phys. Rev. **124**, 340 (1961).

[7] J. B. Grun, M. Sieskind, and S. Nikitine, Détermination de l'intensité d'oscillateur des raies de la série verte de Cu_2O aux basses températures, J. Phys. Radium **22**, 176 (1961).

[8] S. Nikitine, Experimental investigations of exciton spectra in ionic crystals, Philos, Mag, **4**, 1 (1959).

[9] J. Grun and S. Nikitine, Étude de la forme des raies des séries jaune et verte de la cuprite, J. Phys. **24**, 355 (1963).

[10] P. Rommel, P. Zielinski, and J. Main, Green exciton series in cuprous oxide, Phys. Rev. B **101**, 075208 (2020).

[11] N. Moiseyev, Quantum theory of resonances: Calculating energies, widths and cross-sections by complex scaling, Phys. Rep. **302**, 212 (1998).

[12] P. Zielinski, P. Rommel, F. Schweiner, and J. Main, Rydberg excitons in electric and magnetic fields obtained with the complex-coordinate-rotation method, J. Phys. B **53**, 054004 (2020).

[13] P. Grünwald, M. Aßmann, J. Heckötter, D. Fröhlich, M. Bayer, H. Stolz, and S. Scheel, Signatures of Quantum Coherences in Rydberg Excitons, Phys. Rev. Lett. **117**, 133003 (2016).

[14] M. Khazali, K. Heshami, and C. Simon, Single-photon source based on Rydberg exciton blockade, J. Phys. B: At., Mol. Opt. Phys. **50**, 215301 (2017).

[15] V. Walther, R. Johne, and T. Pohl, Giant optical nonlinearities from Rydberg excitons in semiconductor microcavities, Nat. Commun. **9**, 1309 (2018).

[16] S. O. Krüger and S. Scheel, Interseries transitions between Rydberg excitons in Cu_2O, Phys. Rev. B **100**, 085201 (2019).

[17] J. M. Luttinger, Quantum Theory of Cyclotron Resonance in Semiconductors: General Theory, Phys. Rev. **102**, 1030 (1956).

[18] F. Schweiner, J. Main, G. Wunner, and C. Uihlein, Even exciton series in Cu_2O, Phys. Rev. B **95**, 195201 (2017).

[19] R. Knox, *Theory of Excitons*, Solid State Physics: Supplement (Academic, New York, 1963).

[20] C. Uihlein, D. Fröhlich, and R. Kenklies, Investigation of exciton fine structure in Cu_2O, Phys. Rev. B **23**, 2731 (1981).

[21] D. Fröhlich, R. Kenklies, C. Uihlein, and C. Schwab, Assignment of the Even-Parity Excitons in Cu_2O, Phys. Rev. Lett. **43**, 1260 (1979).

[22] G. M. Kavoulakis, Y.-C. Chang, and G. Baym, Fine structure of excitons in Cu_2O, Phys. Rev. B **55**, 7593 (1997).

[23] F. Schöne, S.-O. Krüger, P. Grünwald, M. Aßmann, J. Heckötter, J. Thewes, H. Stolz, D. Fröhlich, M. Bayer, and S. Scheel, Coupled valence band dispersions and the quantum defect of excitons in Cu_2O, J. Phys. B: At., Mol. Opt. Phys. **49**, 134003 (2016).

[24] P. Schmelcher and L. S. Cederbaum, Regularity and chaos in the center of mass motion of the hydrogen atom in a magnetic field, Z. Phys. D: At., Mol. Clusters **24**, 311 (1992).

[25] F. Schöne, S.-O. Krüger, P. Grünwald, H. Stolz, S. Scheel, M. Aßmann, J. Heckötter, J. Thewes, D. Fröhlich, and M. Bayer, Deviations of the exciton level spectrum in Cu_2O from the hydrogen series, Phys. Rev. B **93**, 075203 (2016).

[26] J. W. Hodby, T. E. Jenkins, C. Schwab, H. Tamura, and D. Trivich, Cyclotron resonance of electrons and of holes in cuprous oxide, Cu_2O, J. Phys. C **9**, 1429 (1976).

[27] H. E. Swanson and R. K. Fuyat, Standard X-ray diffraction powder patterns, *National Bureau of Standards Circular No. 539 II* (U.S. Government Printing Office, Washington, DC, 1953), p. 23.

[28] *Landolt-Börnstein–Group III Condensed Matter*, edited by O. Madelung, U. Rössler, and M. Schulz (Springer-Verlag, Berlin/Heidelberg, 1998).

[29] W. P. Reinhardt, Complex coordinates in the theory of atomic and molecular structure and dynamics, Annu. Rev. Phys. Chem. **33**, 223 (1982).

[30] Y. K. Ho, The method of complex coordinate rotation and its applications to atomic collision processes, Phys. Rep. **99**, 1 (1983).

[31] M. A. Caprio, P. Maris, and J. P. Vary, Coulomb-Sturmian basis for the nuclear many-body problem, Phys. Rev. C **86**, 034312 (2012).

[32] R. B. Lehoucq, D. C. Sorensen, and C. Yang, *ARPACK Users' Guide* (Society for Industrial and Applied Mathematics, Philadelphia, PA, 1998).

[33] E. Anderson, Z. Bai, C. Bischof, S. Blackford, J. Demmel, J. Dongarra, J. Croz, A. Greenbaum, S. Hammarling, and A. McKenney, *LAPACK Users' Guide*, 3rd ed. (Society for Industrial and Applied Mathematics, Philadelphia, PA, 1999).

[34] F. Schweiner, J. Ertl, J. Main, G. Wunner, and C. Uihlein, Exciton-polaritons in cuprous oxide: Theory and comparison with experiment, Phys. Rev. B **96**, 245202 (2017).

[35] T. N. Rescigno and V. McKoy, Rigorous method for computing photoabsorption cross sections from a basis-set expansion, Phys. Rev. A **12**, 522 (1975).

[36] Y. Toyozawa, Theory of line-shapes of the exciton absorption bands, Prog. Theor. Phys. **20**, 53 (1958).

[37] G. Koster, J. Dimmock, R. Wheeler, and H. Statz, *Properties of the Thirty-Two Point Groups*, Massachusetts Institute of Technology Press Research Monograph (MIT, Cambridge, MA, 1963).

[38] D. Fröhlich, A. Nöthe, and K. Reimann, Observation of the Resonant Optical Stark Effect in a Semiconductor, Phys. Rev. Lett. **55**, 1335 (1985).

[39] M. Jörger, E. Tsitsishvili, T. Fleck, and C. Klingshirn, Infrared absorption by excitons in Cu_2O, Phys. Status Solidi B **238**, 470 (2003).

[40] J. Schmutzler, D. Fröhlich, and M. Bayer, Signatures of coherent propagation of blue polaritons in Cu_2O, Phys. Rev. B **87**, 245202 (2013).